Journal of Polymers and the Environment (2025) 33:2249–2266
https://doi.org/10.1007/s10924-025-03520-9

ORIGINAL PAPER

Novel and Highly Efficient Antibacterial PLA Composites Prepared with *Liquidambar Orientalis* Oil and Ag@g-C_3N_4 Nanocomposite

Zehra Durmus[1,2] · Roberto Köferstein[3] · Arzu Özgen[4] · Titus Lindenberg[5] · A. Wouter Maijenburg[3,5] · Ali Durmus[6]

Accepted: 28 January 2025 / Published online: 18 February 2025

Abstract

Flexible PLA-based antibacterial composite films were prepared using a natural oil, *Liquidambar orientalis*, as bio-based plasticizer, and 2D graphitic carbon nitride (g-C_3N_4) decorated with Ag nanoparticles with a particle size of 10–30 nm as antibacterial agent (Ag@g-C_3N_4). This structurally designed antibacterial nanocomposite was synthesized with the preparation of g-C_3N_4 by high-temperature annealing followed by the reduction of silver salt onto g-C_3N_4. The Ag@g-C_3N_4 nanocomposite exhibited a surface area value of 18 g/m^2. PLA/Ag@g-C_3N_4 composite films were prepared with solution casting method by introducing 30 phr of *L. orientalis* oil and various amounts (1, 2 and 4 phr) of Ag@g-C_3N_4. It was found that 30 phr of *L. orientalis* oil successfully plasticized the PLA and reduced its glass transition temperature from 60 °C to 43 °C and its melting temperature more than 10 °C by reducing the strong interactions and hydrogen bonds between PLA chains. *L. orientalis* oil also acted as a dispersion agent for the Ag@g-C_3N_4 nanocomposite particles and significantly improved their antibacterial activity. Antibacterial tests performed using Gram-positive bacteria (*Staphylococcus aureus ATCC 25923*) and Gram-negative bacteria (*Escherichia coli ATCC 25922* and *Acinetobacter baumannii ATCC BAA 747*) indicated that introducing a small amount of 2D Ag@g-C_3N_4 nanocomposite particles into PLA yielded superior antibacterial activity.

Keywords Polylactic acid · Antibacterial Composite · Graphitic Carbon Nitride (g-C_3N_4) · Silver (Ag) Nanoparticle · *Liquidambar orientalis*

Introduction

Polylactic acid (PLA) is a thermoplastic polyester and the most extensively used biodegradable plastic in various applications such as textile and medical technologies, automotive plastics, electronics, and mainly in food packaging, due to its superior structural and physical properties [1]. The most prominent advantages of PLA are its biodegradability, good transparency, mechanical durability and easy processing like other commodity thermoplastics. These features make PLA and PLA-based compounds promising and green alternatives to commercially used packaging polymers; polyethylene and polypropylene. However, it is also a well-known fact that the relatively high glass transition temperature (T_g) of PLA (about 60 °C) makes this polymer very brittle in very wide range of temperature and limits its application potential for the areas required flexibility. Therefore, a considerable research effort has emerged to reduce the T_g of PLA and expand its application areas by compounding with different plasticizers, polymers, and additives [2–12]. Majority of

✉ Ali Durmus
durmus@iuc.edu.tr

1 Faculty of Engineering and Natural Sciences, Department of Biomedical Engineering, Biruni University, Istanbul 34015, Türkiye

2 Biruni University Research Center (BAMER), Biruni University, Istanbul 34015, Türkiye

3 Inorganic Chemistry, Institute of Chemistry, Martin Luther University Halle-Wittenberg, 06120 Halle (Saale), Germany

4 Vocational School of Health, Istanbul Gelisim University, Istanbul 34310, Türkiye

5 Center for Innovation Competence (ZIK) SiLi-nano®, Martin Luther University Halle-Wittenberg, 06120 Halle (Saale), Germany

6 Faculty of Engineering, Department of Chemical Engineering, Istanbul University-Cerrahpasa, 34320 Avcılar/Istanbul, Türkiye

commercially available plasticizers used in polymer industry, are synthetic chemicals obtained from petrochemicals and thus crude-oil feed stocks. Regarding the recent trends in chemistry and materials science such as sustainability, environmental friendly materials and processes, and reducing carbon foot-print etc., nontoxic and green plasticizers and additives obtained from biodegradable and renewable resources have been attracted a great scientific and technical attention. Mele et al. used cardanol oil as a bio-based plasticizer in PLA obtained from a renewable resource, cashew agro-industry [13]. Carpintero et al. showed that egg yolk oil acted as a plasticizer for PLA and increased its flexibility and also provided the PLA films antioxidant and light barrier properties [14]. Hasanoglu et al. recently reported that *L. orientalis* oil as a nontoxic, environmentally friendly, and green additive can be successfully used as a natural, renewable, and sustainable plasticizer to produce flexible PLA parts [15]. They also informed about the planting of Anatolian sweetgum trees, harvesting of *L. orientalis* gum and oil, and biochemical and physical features of oil.

Green plasticizers can contribute to produce completely biodegradable PLA compounds. But, functional additives must be introduced into polymer compounds to manufacture parts for particular applications. Antibacterial plastics have been attracted great industrial demands in several applications such as producing synthetic fibers, textiles, and fabrics, food packaging materials, medical parts. Silver nanoparticles and their derivatives are the most extensively and favorably used antibacterial agents in thermoplastics as well as paints, surface coatings, and fibers [16–18]. Several studies have been reported about the preparation, characterization, and specifically food packaging applications of antibacterial PLA-based compounds and composites [19, 20]. Yalcinkaya et al. synthesized Ag grafted cellulose nanocrystals (Ag-g-CNC) and loaded this hybrid filler into PLA [21]. They compared the antibacterial activities of PLA nanocomposites containing 1% wt. of CNC (PLA/1CNC), 0.5% wt. of Ag nanoparticles (PLA/0.5Ag) and hybrid system containing CNC and Ag in the same amount (PLA/1CNC/0.5Ag). They found that the Ag-g-CNC positively affected the thermal degradation and cold crystallization of PLA and the hybrid filler loaded nanocomposite (PLA/1CNC/0.5Ag) showed the best antibacterial performance. Velásquez et al. reviewed the processing techniques used to develop active PLA packaging films included various active agents (AAs), such as essential oils and polyphenols as antibacterial and antioxidant natural compounds and compared their feasibility, advantages, limitations, and relevant processing aspects [22].

In this study, antibacterial and flexible PLA films were prepared using 30 phr of *L. orientalis* oil as natural plasticizer and various amounts (1, 2, and 4 phr) of Ag nanoparticle decorated g-C_3N_4 as antibacterial agent. Structural, physical, and thermal properties of Ag@g-C_3N_4 nanocomposite and PLA/Ag@g-C_3N_4 composite films were studied, in detail.

Experimental

Materials

Melamine (Alfa-Aesar), N,N-Dimethylformamide (Merck), $AgNO_3$ (Carl Roth), $NaBH_4$ (Chemsolute), and Polyvinylpyrrolidone (Carl Roth) were analytical reagent grades and used as received without further purification. Poly (lactic acid) (PLA) was a commercial grade polymer, Luminy®L130, with a melt flow index (MFI) of 10 g/10 min (190 °C, 2.16 kg), density of 1.24 g/cm^3, and L-isomer of 99%, kindly supplied by Amco Polymers, LLC. The *L. orientalis* oil was kindly provided from a local herbalist and essential oil producer in Muğla Province, Turkey. Chemical composition and some other properties of *L. orientalis* oil used in this study was previously reported, in detail [15].

Synthesis and Preparation Studies

Synthesis of Graphitic Carbon Nitride (g-C3N4)

Graphitic carbon nitride (g-C_3N_4) was synthesized according to the previously reported route [23]. In the synthesis, a proper amount of melamine was dispersed into a diluted H_2SO_4 solution. The suspension was placed into a Teflon-lined stainless-steel autoclave and heated up to 180 °C and kept at this temperature for 12 h. Then, the acid-treated melamine precursor was cooled to room temperature and washed repeatedly with distilled water and ethanol. After drying at 80 °C for 12 h, it was heated up to 550 °C in a muffle furnace (Carbolite P310) with a heating rate of 2 °C/min and kept at this temperature for 4 h. Afterwards, the resulting pale yellow g-C_3N_4 powder was obtained.

Synthesis of Ag Decorated g-C3N4 Nanocomposite (Ag@g-C3N4)

Silver (Ag) nanoparticle decorated graphitic carbon nitride (g-C_3N_4) was synthesized following a previously reported procedure [24, 25]. 0.2 g of g-C_3N_4 was added into a flask containing 20 mL of an aqueous solution containing 0.04 mmol $AgNO_3$, which was then vigorously stirred on a magnetic stirrer at room temperature for 24 h. Then, a fresh aqueous solution containing sodium borohydride ($NaBH_4$) was added dropwise into the mixture at 0 °C under vigorous stirring (molar concentration ratio of $AgNO_3$:$NaBH_4$ = 1:50). A

proper amount of poly(vinyl pyrolidone) (PVP), as steric capping agent, was used as a surface stabilizer for reducing the aggregation. The resulting material, g-C_3N_4 flakes decorated with Ag nanoparticles, was obtained by centrifugation and washed with distilled water and dried in vacuum at 100 °C for 12 h.

Preparation of Polylactic Acid (PLA)/Ag@g-C3N4 Composites

PLA films plasticized with *L. orientalis* oil were prepared with solution mixing method. Sample notation and compositions are defined in Table 1. Before the sample preparation, PLA granules were dried in an oven for 24 h at 80 ºC.

In the solution mixing method, PLA was completely dissolved in chloroform (polymer: solvent ratio of 1:10, w/v) then proper amount of *L. orientalis* oil (denoted as L in the sample names) was introduced into PLA solution and rigorously mixed at ambient temperature for 3 h. In another beaker, Ag@g-C_3N_4 powder (denoted as Ag in the sample names) was completely dispersed into a chloroform using ultrasonic homogenizer (Bandelin Sonopuls HD2200) equipped with a horn and KE76 probe with titanium flat tip, for 5 min. Then the PLA solution were gradually poured into the Ag@g-C_3N_4 suspension in 4 parts within one hour and under a vigorous stirring on a magnetic stirrer (300 rpm) at room temperature. A short and intense ultrasonication (2 min.) was also applied to the final mixture to ensure uniform dispersion of particles then the mixture was immediately poured in petri dishes and kept at room temperature for 3 days for evaporating solvent slowly. PLA films were dried in a vacuum oven at 60 °C for 24 h for completely evaporating remaining solvent. A blank PLA film (L0) was also prepared as control sample.

Analysis and Testing Studies

Structural Characterization of Ag@g-C3N4 Nanocomposite

Chemical structures of samples were characterized with Fourier-Transform Infrared Spectroscopy (FTIR) (Tensor 27, Bruker Co.) equipped with an ATR (Attenuated Total Reflectance) device.

Table 1 Sample notations and compositions

Samples	PLA	L. orientalis oil (L)	Ag@g-C_3N_4 (Ag)
L0	100	-	-
L30		30	-
L30-Ag1		30	1
L30-Ag2		30	2
L30-Ag4		30	4
L0-Ag4		-	4

The chemical composition of the samples was determined by an X-ray diffractometer (XRD, Bruker D8 Advance, Cu-Kα, λ = 0.15406 nm, 40 kV, 40 mA) in the 2θ range of 5°−70° with a constant shutter speed, a time step of 0.5 s and a step size of ca. 0.01°. The powders were measured on a silicon (Si) sample holder to reduce the background. The software DiffracPlus EVA. Bruker was used for data evaluation and background correction.

The specific surface area was determined using nitrogen physisorption and five-point Brunauer-Emmett-Teller (BET) method (Nova 1000, Quantachrome Corporation).

Thermal properties of samples were analyzed in a thermogravimetric analyzer (TGA, Netzsch Jupiter STA 449F5) with a heating rate of 10 °C/min under air atmosphere with a flow rate of 50 mL/min.

Morphological and Microstructural Characterization of PLA/Ag@g-C3N4 Composites

Infrared spectra of PLA and composite samples were recorded with a Fourier-transform infrared spectrophotometer (FT-IR, Perkin Elmer Spectrum II) equipped with an ATR (Attenuated Total Reflection) unit in the wavenumber range of 4000–400 cm^{-1} at room temperature to characterize possible reactions and physical and/or chemical interactions between the components.

The morphological features and microstructural properties of the powder and film samples were investigated by a scanning electron microscope (SEM, Carl Zeiss Merlin) and a field emission scanning electron microscope (FE-SEM, FEI Quanta FEG 450) operated at 10 kV, respectively. Cryo-fractured cross-sections of the films were prepared by using liquid nitrogen, after which they were directly prepared by golf sputtering and imaged in the electron microscope.

Contact angle measurements were performed with a KSV Attension®, Theta Lite Goniometer device using the pendant drop method (5 µL of water) taken at least five points on the film sample.

Melting and Crystallization Behaviors of PLA/Ag@g-C3N4 Composites

Thermal behaviors of samples were investigated using a differential scanning calorimeter (SII Nanotechnology, Hitachi ExStar 6200) equipped with an electrical cooling device (Thermo-Scientific intracooler: EK90C/SII). Calibration of the instrument was conducted using indium (In), tin (Sn), and zinc (Zn) metals. Samples weighing 7–8 mg in an aluminum pan were heated from 0 °C to 220 °C with a heating rate of 10 °C/min and equilibrated at this temperature for 3 min to eliminate thermal history. The samples were then cooled to 0 °C with a cooling rate of 30 °C/min and kept at

this temperature for 3 min. Finally, they were heated up to 220 °C with a heating rate of 10 °C/min. DSC runs were performed under nitrogen atmosphere with a flow rate of 50 mL/min, to avoid thermo-oxidative degradation. Degree of crystallinity (X_c, %) values of samples were calculated using the following equation;

$$\%X_c = \frac{\Delta H_m}{\Delta H_m^0(1-\alpha)} x100 \quad (1)$$

where ΔH_m is the melting enthalpy of samples (J/g) recorded during second heating, ΔH^o_m is the melting enthalpy value of 100% crystalline form of PLA (93.6 J/g) [26], and α is the sum of the weight fractions of plasticizer and additive (*L. orientalis* oil and Ag@g-C_3N_4).

Dynamic Mechanical Analysis of PLA/Ag@g-C3N4 Composites

Solid state viscoelastic properties of samples were analyzed with a test protocol performed in a dynamic mechanical analyzer (DMA, SII Nanotechnology, Hitachi, ExStar DMS 6100). The temperature sweep test was performed in uniaxial tension mode with a heating rate of 3 °C/min and frequency of 1.0 Hz in the temperature range of 20–160 °C. Rectangular film specimens with dimensions of 20 × 5 × 0.2 mm were used.

Antibacterial Tests

Bacterial strains.

In the antibacterial activity assays, we used Gram-positive bacteria (*Staphylococcus aureus* ATCC 25923) and Gram-negative bacteria (*Escherichia coli* ATCC 25922 and *Acinetobacter baumannii* ATCC BAA 747), which were stored in our laboratory.

Disc Diffusion Method.

The disc diffusion method was used to determine the antibacterial activities of composite films. The samples were tested on three types of bacteria, including *S. aureus* ATCC 25,923, *E. coli* ATCC 25,922, and *A. baumannii* ATCC BAA 747. PLA film and L30 (PLA film containing LO essential oil) were used as negative controls, while VA: vancomycin (30 µg/ml), AMC: amoxicillin-clavulanate (20/10 µg/ml), and AMC: amoxicillin-clavulanate (20/10 µg/ml) were used as positive controls for each respective bacteria type. First, a 10^8 CFU/mL dilution was prepared by growing microorganisms in Luria-Bertani liquid media (Merck) for 16 h. The concentration was then adjusted to correspond to a 0.5 McFarland concentration, and this dilution was used as the inoculum. Next, 60 µl of the bacterial dilution was added to petri dishes containing Luria-Bertani (Merck) agar and spread using an L-loop stick. The films were prepared as square pieces with 6 mm edges, sterilized under UV irradiation (both sides) for 20 min, and placed appropriately in petri dishes. The petri dishes were then incubated at 37 °C for 24 h, and the diameters of inhibition zones were measured in millimeters. The experiments were repeated thrice to ensure accuracy [27, 28].

Results and Discussion

Structural Characterizations of Ag@g-C3N4 Nanocomposite

Figure 1(a) and 1(b) show the FT-IR spectra of pristine g-C_3N_4, Ag@g-C_3N_4, and Ag@g-C_3N_4 after heating at 340 °C as TGA residue in different wavenumber range. All samples exhibit the characteristic structure of g-C_3N_4. Each sample shows an absorption peak around 810 cm^{-1}, indicating the presence of a tri-s-triazine-based structure. The peaks observed in the 1200–1700 cm^{-1} range correspond to the typical stretching vibrations of C-N heterocycles. Additionally, peaks near 3400 cm^{-1} are attributed to N-H and O-H stretching vibrations, which imply amino groups and adsorbed water. A comparison between and the TGA residue at 340 °C (intermediate) shows the disappearance of bands at 1570, 1534, 1453, and 1308 cm^{-1}. This result indicates that the heating yields change in the Ag@g-C_3N_4 structure. The TGA residue after full decomposition at 900 °C only shows reflections of silver and the broad reflection at 28° disappears, which supports the assumption that the peak originated from g-C_3N_4.

Figure 1(c) compares the XRD patterns of pristine g-C_3N_4, Ag@g-C_3N_4, intermediate residue of Ag@g-C_3N_4 (black-brown powder after heating up to 340 °C in TGA), and final residue of Ag@g-C_3N_4 (white shining powder after heating up to 900 °C in TGA). Pristine g-C_3N_4 exhibits two broad crystallinity peaks indexed (100) at 13° and (002) at 28° with PDF #01–087–1523 in the DiffracPlus Eva software library. These broad peaks could be attributed to the fact that the strong acid treatment partially destroys the graphitic structure and produces some fragments in the g-C_3N_4 sample [23]. It is seen that the XRD pattern of intermediate residue is identical to the pattern of Ag@g-C_3N_4 and shows strong reflections of elemental silver. The very broad and weak peak of intermediate, observed at 28°, indicates low crystalline g-C_3N_4. This peak is completely disappeared after heating the Ag@g-C_3N_4 up to 900 °C because all the organic content (carbon nitride structure) is decomposed. It was also obtained that peak (100) at 13° seemed in the pristine g-C_3N_4 and appeared in none of Ag@g-C_3N_4, intermediate, and final residues. This result could be attributed

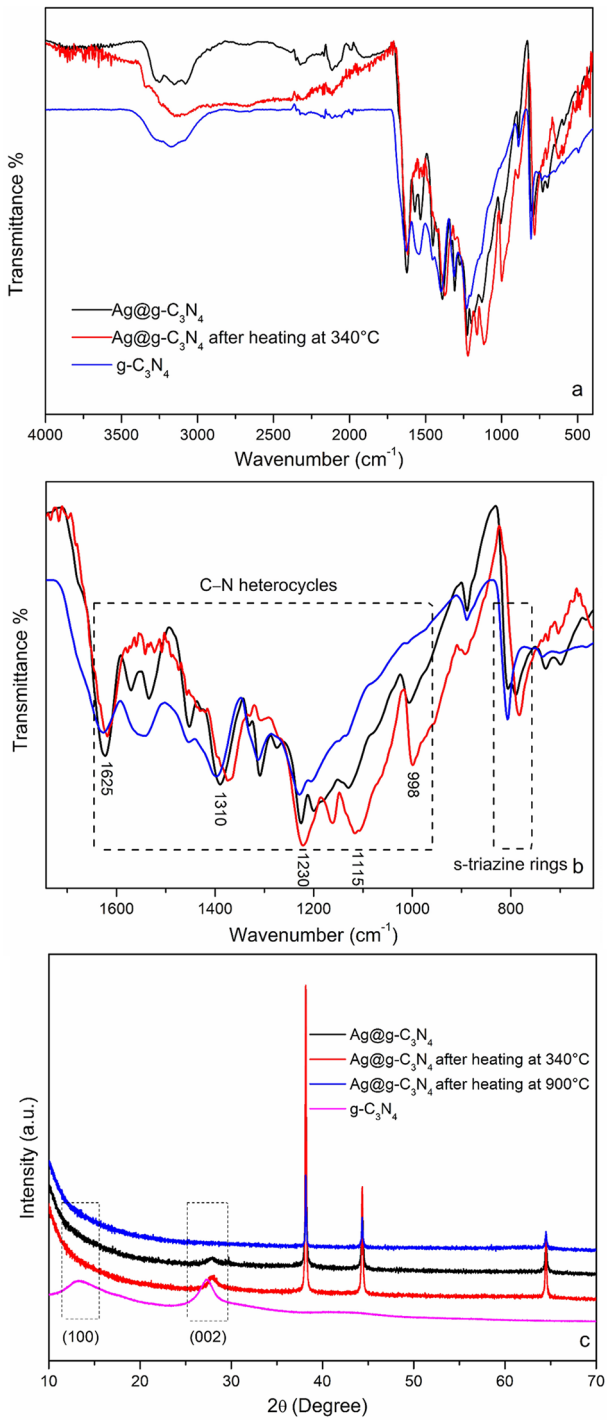

Fig. 1 (a) Full scale FTIR spectra of g-C_3N_4, Ag@g-C_3N_4, and Ag@g-C_3N_4 after heating up to 340 °C, (b) focusing their spectra in the wavenumber range of 1700–700 cm^{-1} and (c) XRD patterns of g-C_3N_4, Ag@g-C_3N_4, and Ag@g-C_3N_4 after heating up to 340 °C and 900 °C

to the same issue that the low crystalline g-C_3N_4 shows a strong preferred orientation in the Ag@g-C_3N_4 structure thus the (100) peak is not appeared. Some researchers also concluded that the Ag introducing into the g-C_3N_4 matrix may disturb the g-C_3N_4 structure by altering the in-plane structural repeating network [29–31].

Morphologies of g-C_3N_4 and Ag@g-C_3N_4 nanocomposite are given in Fig. 2. SEM images of g-C_3N_4 clearly implies that it is formed with layered structure. These curved layers, showing a convex and spherical form in many parts and having a few tens nanometer in thickness are stacked to form macro pores with larger diameter than a few hundreds. Surface of layers are quite smooth while the cracked edges of stacks includes some roughness. On the other hand, SEM images of Ag@g-C_3N_4 nanocomposite is highly different from the pristine g-C_3N_4. As especially seen in the SEM image below on the right, Ag nanoparticles (as shiny white points) and agglomerates are distributed well onto the surface of g-C_3N_4. It can be assumed that the size of Ag nanoparticles varied in a wide range, approximately in 10–30 nm.

Based on the BET measurements, surface area values of g-C_3N_4 and Ag@g-C_3N_4 were determined to be 25 and 18 m^2/g, respectively. It was found that the decoration of g-C_3N_4 surfaces with silver nanoparticles yielded only to a small reduction in its specific surface area probably due to the blocking of mesopores with largely agglomerated Ag nanoparticles.

Figure 3 represents the TGA, DTG, and DSC thermograms of pristine and Ag decorated g-C_3N_4. Figure 3(a) shows that the g-C_3N_4 is stable in air up to 580 °C. Further heating leads to a decomposition process with a strong weight loss of 80%. The decomposition process is completed at approximately 730 °C. The 20% residue is probably caused by oxygen capturing from air onto the protonated surfaces, as pointed out in our recent paper [23]. In general, the thermo-oxidative decomposition of g-C_3N_4 roughly remains a 10% residue [32]. In this study, the Ag@g-C_3N_4 nanocomposite shows a different decomposition behavior. The first weight loss step about 7.1% appeared in the temperature range of 200–300 °C probably corresponds to decomposition of organic compound (PVP) used as steric capping agent. Intermediate Ag@g-C_3N_4 is stable up to 410 °C then the second two-step decomposition begins above 410 °C and proceeds to 540 °C. This second decomposition corresponds to collapsing the structure and formation of volatile carbon and nitrogen species. It was found that the main decomposition process of Ag@g-C_3N_4 begun approximately 120 °C earlier than the g-C_3N_4. It might be originated from the catalytic effect of Ag nanoparticles for the decomposition organic structure because it is a well-known fact that the active metal sites onto a support initiate and accelerate the decomposition behaviors of organic molecules [33]. Total weight loss of nanocomposite was found to be 33.5%. XRD analysis of the residue of Ag@g-C_3N_4 nanocomposite as given in Fig. 1(c) only showed characteristic peaks of Ag;

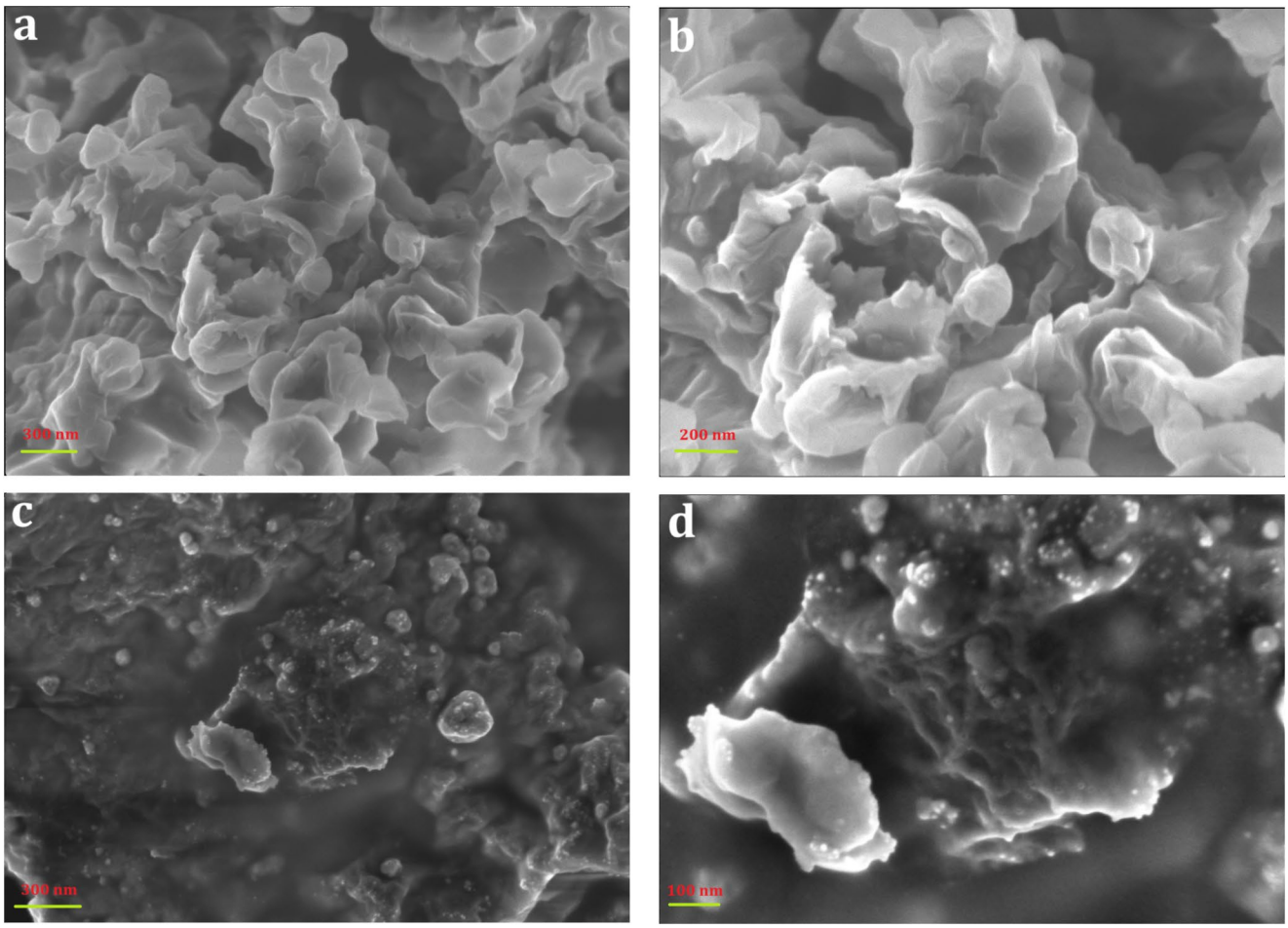

Fig. 2 SEM images of g-C_3N_4 (a and b) and the Ag@g-C_3N_4 nanocomposite (c and d)

(111) at 38.1°, (200) at 44.3°, and (220) at 64.5, indexed as the cubic phase of Ag (JCPDS No. 04–0783), consistently with the literature [34]. DSC thermograms of g-C_3N_4 and Ag@g-C_3N_4 given in Fig. 3(c) display similar peak shapes to their DTG curves and clearly exhibit oxidative decomposition exotherms. It is noticeable that the exotherm of g-C_3N_4 spread over a very wide temperature range, starting at 100 to end up at 750 °C. It should be noted that DSC signal is associated with the change in heat capacity of specimen with temperature. Thus, such an extremely wide range of exotherm is related to the heat capacity change of g-C_3N_4 and the main decomposition exotherm is seen as a sharp and small peak above 700 °C. The DSC thermogram of Ag@g-C_3N_4 implies three distinctive peaks at 300, 440 and 500 °C which correspond to the ends of thermo-oxidative decompositions of PVP, first step of g-C_3N_4 and second step of g-C_3N_4 as mentioned above.

Structural and Morphological Properties of PLA/Ag@g-C3N4 Nanocomposites

Figure 4(a-c) illustrate the photographs of solution casted PLA/Ag@g-C_3N_4 nanocomposite films. It is seen that the neat PLA and PLA plasticized with the *L. orientalis* oil yielded much transparent films compared to the Ag@g-C_3N_4 loaded ones. PLA is more transparent than the plasticized counterpart. It was possibly due to the effect of *L. orientalis* on the dynamics of PLA chains by enhancing the chain mobility thus degree of crystallinity during solvent evaporation and solidification of polymer solution.

One can also notice that the addition of 30 phr *L. orientalis* oil slightly turned the film color into yellowish in addition to the higher opacity. Increase in the loading amount of Ag@g-C_3N_4 resulted in the dark brown color thus the logo image cannot be clearly seen under any of these samples.

Figure 4(d) shows the flexibilities of plasticized PLA with *L. orientalis* oil in the absence and presence of 4 phr of Ag@g-C_3N_4 additive. It was found that the introducing of

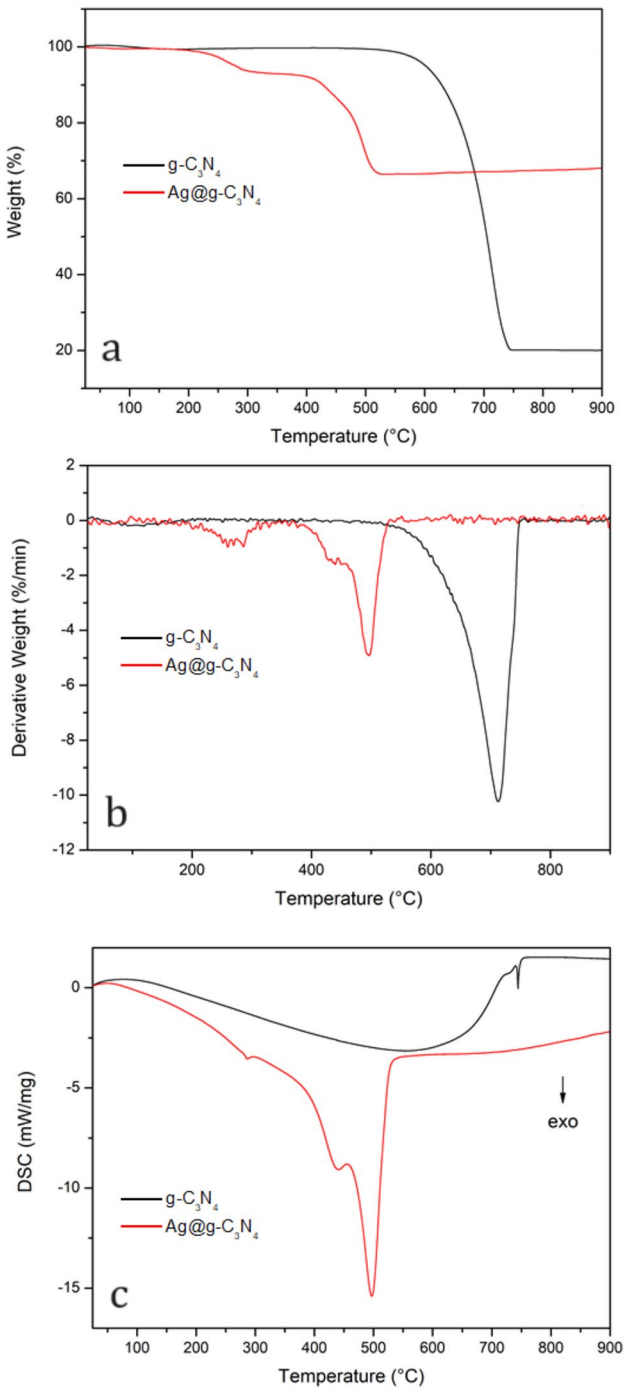

Fig. 3 (a) TGA, (b) DTG, and (c) DSC thermograms of g-C_3N_4 and Ag@g-C_3N_4

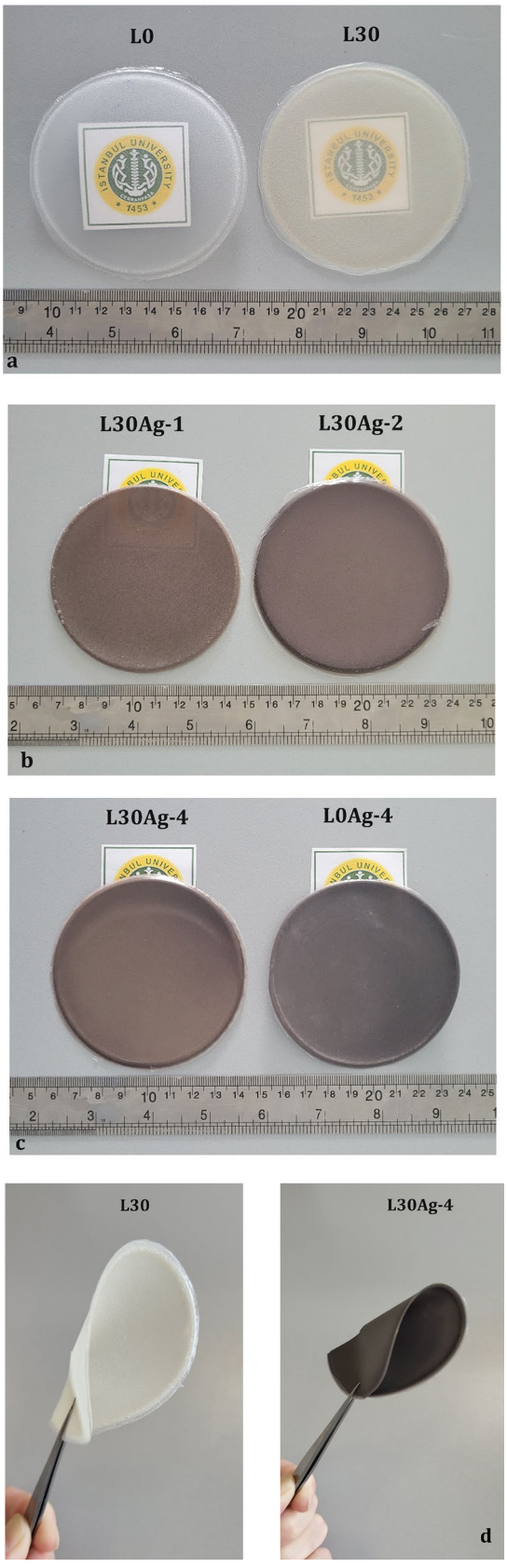

Fig. 4 Photographs of solution casted film samples

a solid functional additive did not inversely affect the flexibility of sample.

Figure 5(a), 5(b), and 5(c) show the FTIR spectra of PLA, *L. orientalis* oil and composite samples, respectively.

FTIR spectra of PLA film shows the characteristic bonds of polymer chain as denoted on the spectrum. The natural plasticizer, *L. orientalis* oil exhibited many characteristic

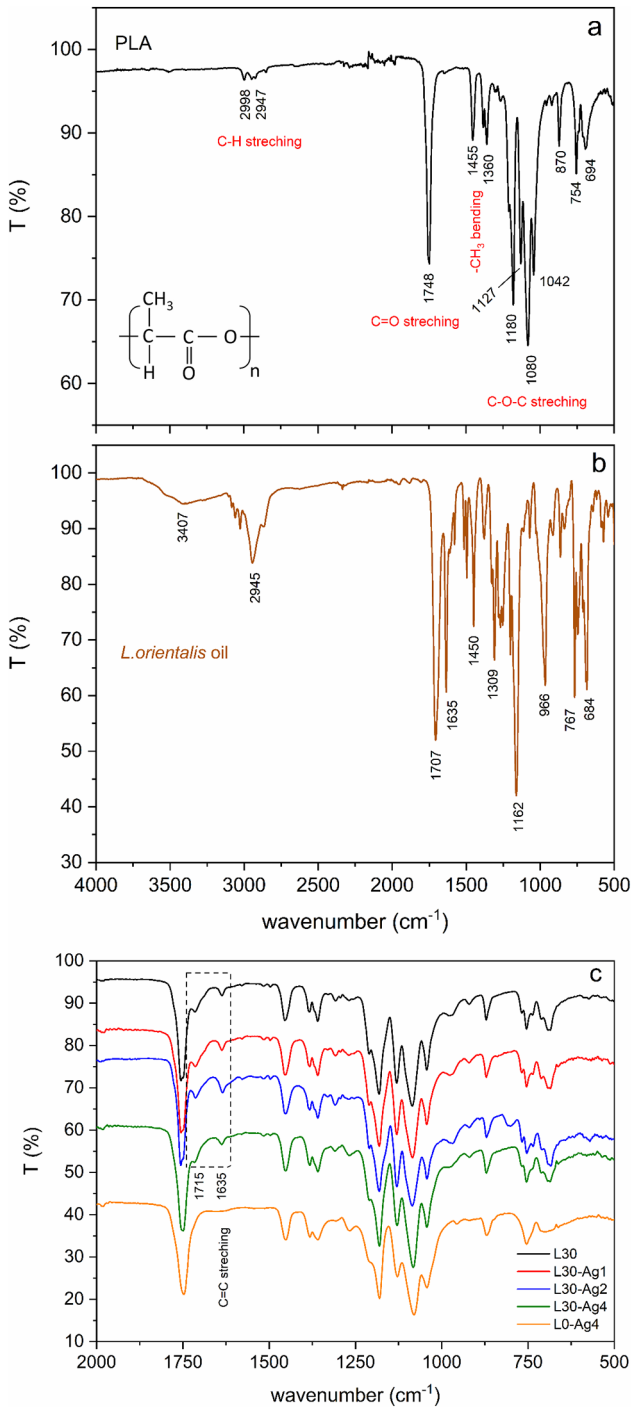

Fig. 5 FTIR spectra of (a) PLA, (b) *L. orientalis* oil, and (c) composite samples

peaks below the wavenumber of 1700 cm^{-1}. Peaks in the range of 1000–650 cm^{-1} and 1650 − 1450 cm^{-1} correspond to vibrations of C = C and C-H bonds of aromatic units, respectively, as previously reported [35, 36]. It was reported that the main components (wt%) of *LO* oil were styrene (70.4%), α-pinene (19.4%), β-pinene (4.3%), and β-caryophyllene (0.2%) [37]. Therefore, the distinctive and characteristic peak of *L. orientalis* oil could be considered as the C = C bond of styrene seen at 1635 cm^{-1}. Figure 5(c) compares the FTIR spectra of composites to the plactized PLA specimen (L30). The peaks appeared at 1715 and 1635 cm^{-1} in FTIR spectra of composites corresponded to ketonic species in the *L. orientalis* oil and C = C bonds of styrene, as the main components of *L. orientalis* oil, respectively. The absence of other new peaks in the spectra of the composite samples pointed out that there was no chemical interaction between the components, PLA, natural plasticizer, and functional nanocomposite. Any characteristic peak (C-Cl strecthing at 773 cm^{-1} and C-Cl bending at 670 cm^{-1}) belong to the solvent, chloroform or trichlorometan ($CHCl_3$), used in film preparation did not detected in the FTIR spectra of PLA and composites. This result indicated that the solvent was completely removed from the samples.

Figure 6 compares the SEM images of cryo-fractured cross-sections of L0(PLA), L30-Ag4, and L0-Ag4 samples taken with the magnification of x5000. It appears that many fracturing points have formed on the surface of L0 but the cross-section of L30-Ag4 possesses a smooth fracturing surface although it includes 4 phr of solid additive. It is also interesting that solid particles are not clearly observed in the SEM image of L30-Ag4 at this magnification. On the other hand, agglomerated particles are clearly observed on the fractured surface of L0-Ag4 which indicates poor dispersion of functional additive. Surface topography of samples implies that the addition of *L. orientalis* oil improves the dispersion of Ag@g-C_3N_4 particles into PLA matrix. Based on the SEM images, it can be concluded that the *L. orientalis* oil acted as a dispersion agent or compatibilizer for the Ag@g-C_3N_4 particles. Therefore, this natural oil might be a dual-function material into PLA-based composites as bio-based plasticizer and dispersion agent.

Figure 7 represents the SEM images of L0, L30 and samples prepared with different amounts of Ag@g-C_3N_4 additive, taken with the magnification of x10.000, except the L30-Ag2 (x5000). This figure also reports the elemental composition of L30-Ag2 sample based on the semi-quantitative EDS analysis on a particular region of sample seen as gray domain at the center of image. Higher magnification SEM images of composites specify the well dispersion of Ag@g-C_3N_4 due to the contributing effect of *L. orientalis* oil to particle dispersion as mentioned before.

It was found that the weight fraction of Ag was 0.82 in the L30-Ag2 sample regarding the EDS analysis. TGA analysis indicated that the g-C_3N_4 ratio of Ag@g-C_3N_4 was about 33.5 wt%. The remaining 66.5 wt% should be silver oxide (Ag_2O) due to easy formation of silver oxide by reacting of elemental silver (Ag) with oxygen above the 200 °C under oxidative atmosphere. Atomic composition of Ag_2O can be transformed into weight ratio; as 93 wt% of silver

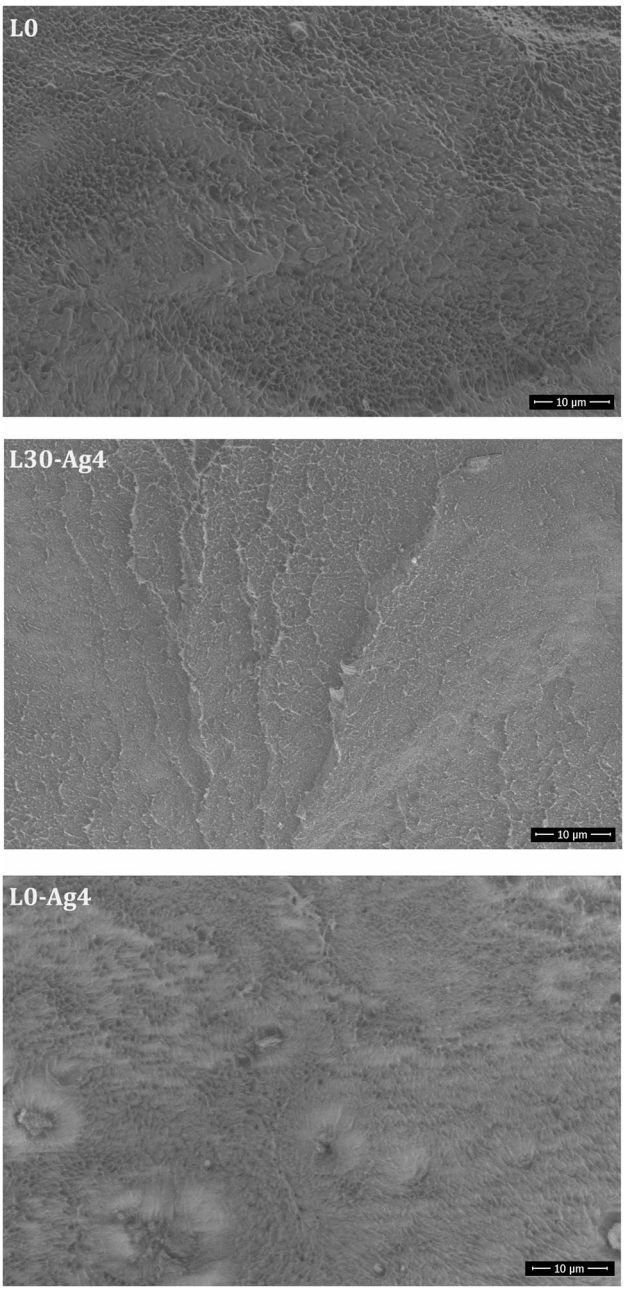

Fig. 6 SEM images of PLA (L0), L30-Ag4, and L0-Ag4

and 7 wt% of oxygen. Considering the weight ratio of Ag_2O and TGA result, it can be determined that that the 93 wt% of remaining amount (66.5 wt% as Ag_2O) should be Ag (about 62 wt%). The weight% of Ag@g-C_3N_4 in the L30-Ag2 sample must be about 1.5 wt% regarding the 2 part of additive in the total 132 part of sample (100 + 30 + 2) and 62 wt% of 1.5 wt% corresponds to 0.93 wt% of Ag. EDS analysis indicated the 0.82 wt% of Ag in this sample. The compositional deviation about 12% can be accepted within the reliable limits for such a semi-quantitative approach and this result confirms the compositional consistency of samples.

Figure 8 shows the representative images of contact angle measurements and the average contact angle values of samples are also listed in Table 2. Contact angle measurements were performed at least five different points on a specimen and the average values of left and right angles were reported with the standard deviations.

The contact angle value of neat PLA film was about 75 that is very consistent with the previously reported values [17, 38, 39]. Addition of 30 phr *L. orientalis* significantly increased the contact angle value of PLA. This increase clearly refers to a substantial improvement in hydrophilicity of PLA as the natural oil is composed of various aromatic and cyclic organic compounds as reported before [15]. It could be assumed that the improvement in hydrophilicity of PLA may reduce its hydrolytic decomposition or biodegradation rate and enhance the physical durability of PLA parts plasticized with *L. orientalis* oil. Introducing of functional additive, Ag@g-C_3N_4, into plasticized specimen decreased the contact angle value of L30. But, the contact angle values of all composites were still quite higher than that of PLA because the amount of *L. orientalis* oil was much higher than the amount of Ag@g-C_3N_4. It was also found that the addition of 4 phr Ag@g-C_3N_4 without natural oil did not change the contact angle value of PLA.

Thermal Properties of PLA/Ag@g-C3N4 Composites

Figure 9(a-c) exhibit the DSC thermograms of samples recorded at first heating, cooling, and second heating cycles. The DSC parameters of samples calculated from corresponding thermograms are also listed in Table 3. In Fig. 9(a), it is seen that all samples exhibit single melting endotherms. During the first heating, none of the samples showed glass transition and cold crystallization peak clearly because all the samples were crystallized during solvent evaporation and solidification process. It is a well-known fact that the first heating run in DSC analysis of polymers is applied for deleting the thermal history of specimens thus excessive and speculative arguments should not be constructed on the first heating thermograms. But, it should be noted that the most interesting and obvious finding about the first heating thermograms is the fact that the melting endotherms of plasticized specimens significantly shift to lower temperatures, about 15 °C compared to the PLA and L30. This decrease can be attributed to plasticization effect of *L. orientalis* oil on PLA, well. Figure 9(b) indicates that none of the samples can crystallize during the relatively fast cooling rate (30 °C/min.). This result implied that all samples formed highly amorphous structure during the cooling step. The T_g values of unplasticized samples, L0 and L0-Ag4, were found to be 52.5 and 52.8 °C, respectively. But, the T_g values of plasticized samples varied in the range of 30–37 °C. This result

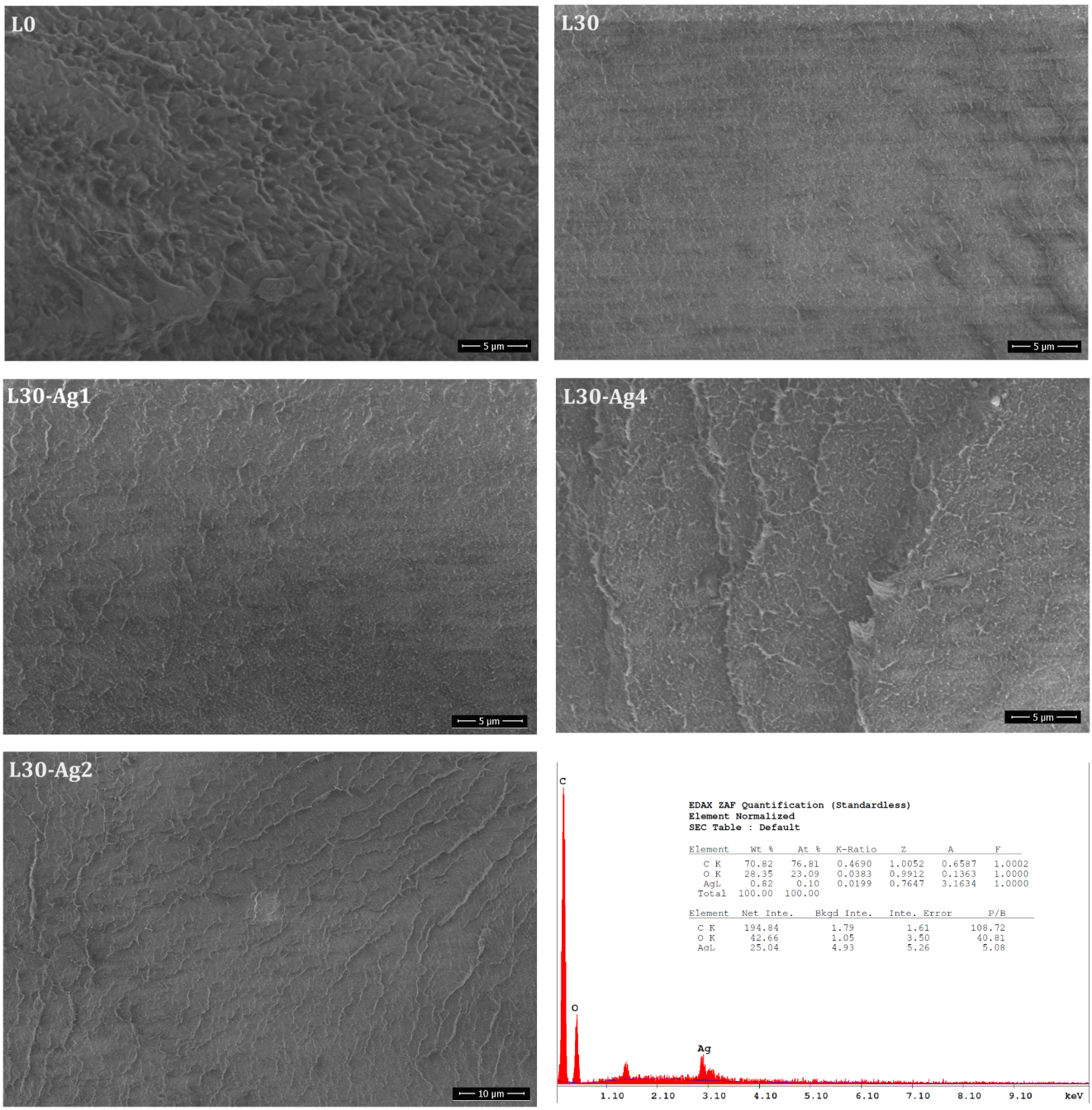

Fig. 7 SEM images of PLA (L0), L30, composites, and EDS results of L30-Ag2

also marks the plasticization effect of *L. orientalis* oil as previously reported [15]. The most quantitative results about the effect of compositional variations on the thermal properties of semi-crystalline thermoplastic based systems can be extracted from the second heating thermograms because the thermal history of polymer chains and processing related microstructural features have been deleted. In Fig. 9(c), it is seen that all samples exhibit glass transition temperature, cold crystallization exotherm and melting endotherm. A smaller, low temperature shoulder can also be noticed in the thermograms of L30-Ag2 and L30-Ag4 samples just before the main melting peak. During the second heating, T_g values of unplasticized specimens, P0 (PLA) and L0-Ag4, were found to be 60.2 and 60.5 °C, respectively. Introducing 30 phr of *L. orientalis* oil into PLA reduced its T_g value about 17 °C. Addition of Ag@g-C_3N_4 into the plasticized PLA resulted in further reduce in glass transition temperature.

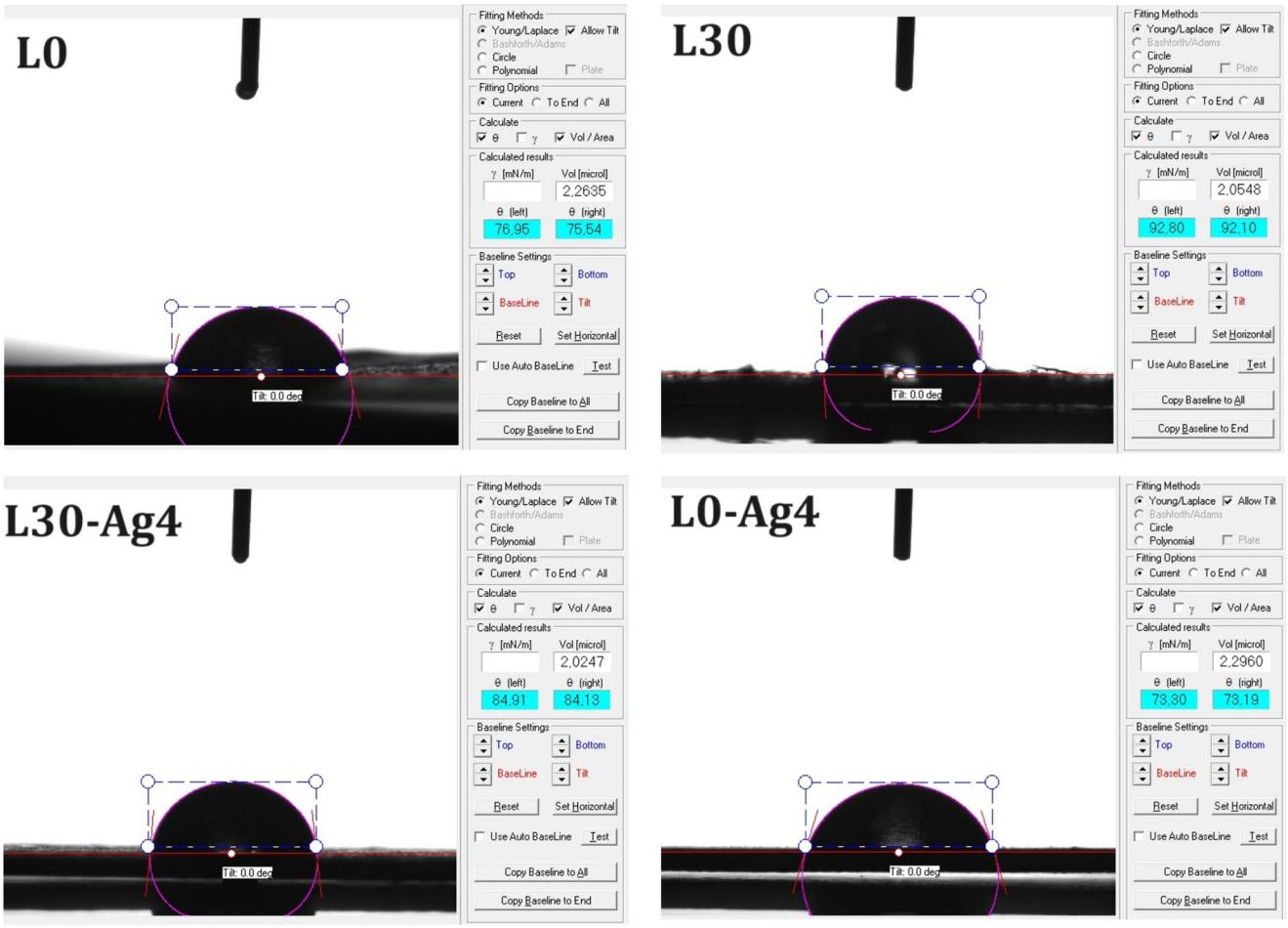

Fig. 8 Representative images for the contact angle measurements of samples

Table 2 Contact angle values of film samples

Samples	Left	Right
L0	75.3 ± 1.30	74.7 ± 0.73
L30	92.9 ± 2.06	91.3 ± 2.69
L30-Ag1	89.8 ± 0.57	88.9 ± 0.89
L30-Ag2	85.6 ± 0.22	83.8 ± 0.44
L30-Ag4	84.9 ± 0.33	84.1 ± 0.56
L0-Ag4	74.3 ± 1.57	74.7 ± 1.61

As seen in Fig. 9(c), PLA exhibited a cold crystallization behavior in the temperature range of 100–135 °C. Similar cold crystallization behavior was also observed for the L0-Ag4. Plasticization of PLA with the *L. orientalis* oil significantly decelerated the cold crystallization of PLA based on the following findings; (i) apparently broadening the cold crystallization exotherm, (ii) shifting the peak maximum temperature ($T_{cc-peak}$) to higher value, and (iii) decreasing the intensity of crystallization exotherm and enthalpy value (ΔH_{cc}). In the specific case of *L. orientalis* oil, Hasanoglu et al. explained this effect by the excellent distribution of aromatic and cyclic compunds of *L. orientalis* oil into the PLA phase and restriction effect of these organic molecules for ordering of PLA chains [15]. It was found that introducing Ag@g-C_3N_4 into the plasticized PLA with 30 phr of *L. orientalis* oil dramatically accelerated the cold crystallization behavior of PLA. Ag@g-C_3N_4 addition led to decrease the crystallization peak onset and peak maximum temperature and increased the crystallization enthalpy values compared to L30. This result can be attributed to the characteristic nucleation effect of 2D solid materials on the phase transition of polymer chains due to the formation of physical network with solid particles and resulting restriction effect for the mobile PLA chains then easy folding into ordered structure. Although the crystallization mechanism of semi-crystalline polymers as the phase transition from unordered (or amorphous) state to ordered state is a well-known phenomenon, dynamics of cold crystallization is quite different from the most commonly discussed melt crystallization issue under non-isothermal conditions because chain folding proceeds with the increase in temperature during cold crystallization. In this transition, the effect of temperature and effect of solid additives on the chain mobility work oppositely. Therefore, it has been accepted that the cold crystallization is a more

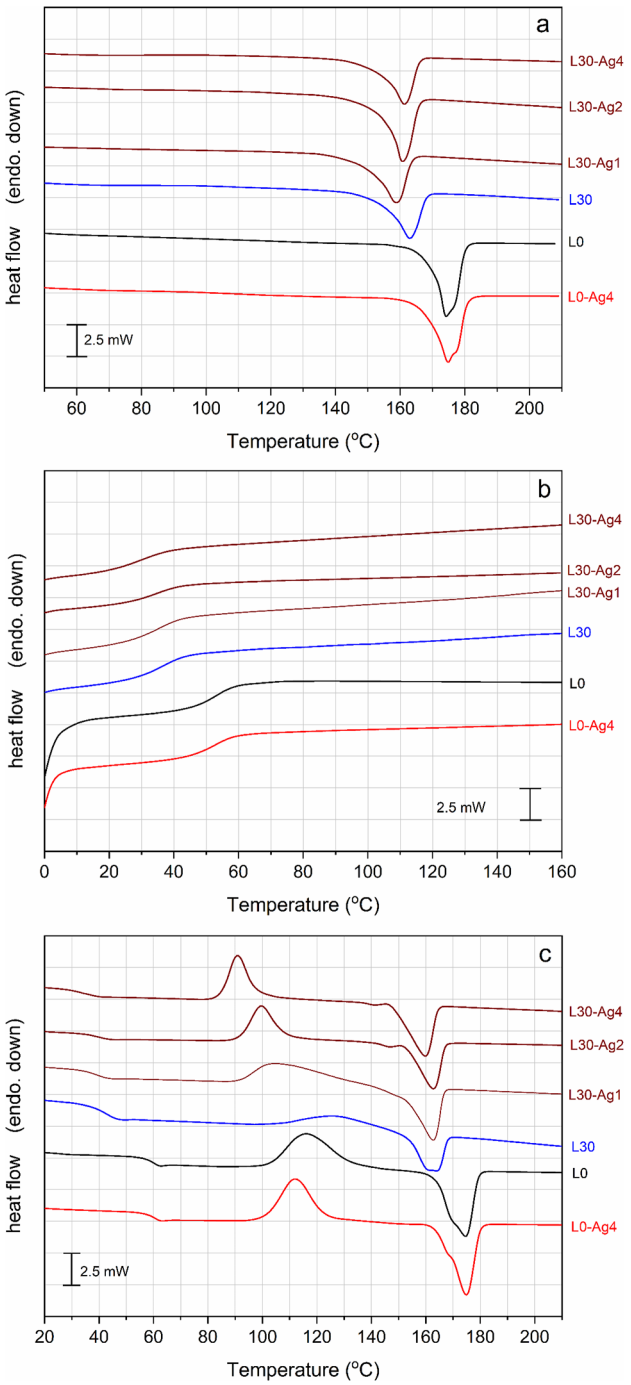

Fig. 9 (a) DSC first heating, (b) cooling, and (c) second heating thermograms of samples

complex phenomenon than the melt crystallization. In this study, both the converse effects of plasticizer (*L. orientalis* oil) and nucleating agent (Ag@g-C_3N_4) on such a complex transition must be taken into account.

Consequently, it has been inferred that these functional additives do not induce the melt crystallization of PLA under fast cooling conditions. This result refers that any

Table 3 DSC parameters of samples

Samples	1st heating		cooling	2nd heating					
	T_m (°C)	ΔH_m (J/g)	T_g (°C)	T_g (°C)	$T_{cc-onset}$ (°C)	$T_{cc-peak}$ (°C)	ΔH_{cc} (J/g)	T_m (°C)	ΔH_m (J/g)	X_c (%)
L0	174.2	38.0	52.5	60.2	101.6	116.1	41.2	174.5	41.5	44.3
L30	163.0	30.6	36.7	43.0	99.2	125.6	10.0	162.4	13	18.1
L30-Ag1	159.0	33.5	35.3	39.6	92.1	104.6	29.6	162.7	33.2	46.5
L30-Ag2	160.8	32.4	35.0	39.4	90.7	99.6	27.0	162.8	32.0	45.1
L30-Ag4	161.3	30.2	30.3	33.3	83.7	90.8	25.6	159.8	28.5	40.8
L0-Ag4	175.0	33.5	52.8	60.5	100.0	112.0	32.0	175.0	34.6	38.4

of these compositions can be solidified in amorphous state with the melt state processing operations such as film blowing or injection molding. But, the composite samples may crystallize when they are exposed to relatively high temperatures about 80 °C. This phenomenon brings about the physical deformations such as shrinking and deflection on parts and changes their physical properties. From the realistic point of view, it can be concluded that a dominantly evident cold crystallization behavior might narrow down the application area and service conditions of PLA-based parts. As concluded for the melting endotherms recorded during the first heating run, it was obtained that the melting temperatures of plasticized samples (L30, L30-Ag1, L30-Ag2, and L30-Ag4) were lower than unplasticized ones (L0 and L0-Ag4) during second heating. Low melting temperature of semi-crystalline polymers can be related to two phenomena; (i) smaller crystal size formed with the thinner lamellas and lower degree of crystallinity values (X_c, %) and/or (ii) lower interactions between chains in folded and ordered domains. Comparing the X_c values of composite samples, calculated with the Eq. 1 and listed in Table 3, it is seen that their degree of crystallinity values are not lower than the L0 and L0-Ag4. This result implies that lower melting temperatures of such samples are obviously originated from the latter case. *L. orientalis* oil can effectively plasticize PLA by reducing the strong interactions and hydrogen bonds between PLA chains and lead to transform easier from ordered solid to melt state than the unplasticized counterparts. This relationship may allow us to expect another role from *L. orientalis* oil as processing aid in melt compounding operations in addition to aforementioned ones; plasticizer and dispersion agent.

Dynamic Mechanical Analysis of PLA/Ag@g-C3N4 Composites

Figure 10(a) shows the storage modulus (E') curves of samples as a function of temperature. As the DMA analyses were performed with the specimens taken from the solution casted samples seen in Fig. 4, DMA thermograms directly reflected the solid state viscoelastic and mechanical properties of samples.

Cold crystallization phenomenon was not observed in the samples because they were already crystallized during solvent evaporation and solidification step. Their X_c% values, calculated with the enthalpy values of samples recorded at first heating and listed in Table 3, were found to be in the range of 40.6–46.9. All the compositional variations yielded a relatively small difference in X_c%. This result pointed out that variation in the viscoelastic and mechanical properties of samples was not related to their different degree of crystallinity values. As these samples do not show cold crystallization behavior, E' values of samples can be compared at rubbery plateau. Figure 10(b) illustrates the comparison of E' values at 100 °C as a function of compositional variation. It is seen that the addition of 30 phr plasticizer decreases the E' of PLA while the addition of 4 phr Ag@g-C_3N_4 without plasticizer increased the modulus. In the plasticized samples, increasing amount of Ag@g-C_3N_4 readily improves the modulus, as expected.

Antibacterial Properties of PLA/Ag@g-C3N4 Composites

Antibacterial activity results of samples on *A. baumannii* ATCC BAA 747, *E. coli* ATCC 25,922, and *S. aureus* ATCC 25,923 are given in Table 4. Additionally, inhibition zones are also shown in Fig. 11.

The antibacterial activity of samples was evaluated using the disk diffusion method. The study revealed that PLA and L30 films did not show any antibacterial activity. However, the unplasticized sample including 4 phr of antibacterial agent (L0-Ag4) exhibited significant antibacterial activity against all types of bacteria tested. The L0-Ag4 film created growth inhibition zones of 11, 11, and 13 mm in diameter on *A. baumannii*, *E. coli*, and *S. aureus* bacteria, respectively. It is worth noting that silver is a well-known antibacterial agent and is widely used in various fields, such as food packaging, medical materials, devices, and cosmetics [31, 40, 41].

It was interestingly found that the L30-Ag1, L30-Ag2, and L30-Ag4 samples showed the same or slightly higher antibacterial activity than L0-Ag4 for *A. baumannii* and *S. aureus*. A similar trend was found for *E. coli*, except the L30-Ag2. Similar or higher antibacterial activity of composites even though lower amount of Ag was probably due to the dispersing agent effect of *L. orientalis* oil as mentioned before based on the SEM images. It can be concluded that the natural plasticizer contributed to antibacterial agent for dispersing well into PLA structure and yielded higher antibacterial activity. L30-Ag1 film resulted in an inhibition zone of 14, 12, and 12 mm against *S. aureus*, *E. coli*, and *A. baumannii* bacteria, respectively. The inhibition zone of L30-Ag2 film against *S. aureus*, *A. baumannii* and *E. coli* bacteria was found to be 13, 11 and 7 mm, respectively. The inhibition zone of the L30-Ag4 film against *S. aureus*, *E. coli* and *A. baumannii* bacteria was found to be 14, 13, and 11 mm respectively.

According to the results, only L. orientalis added and both plasticizer and antibacterial agent loaded samples are more effective on G (+) bacteria than G (-) bacteria. This situation is consistent with the literature [42–45]. G (-) bacteria have lipopolysaccharide (LPS) layers in their cell walls.

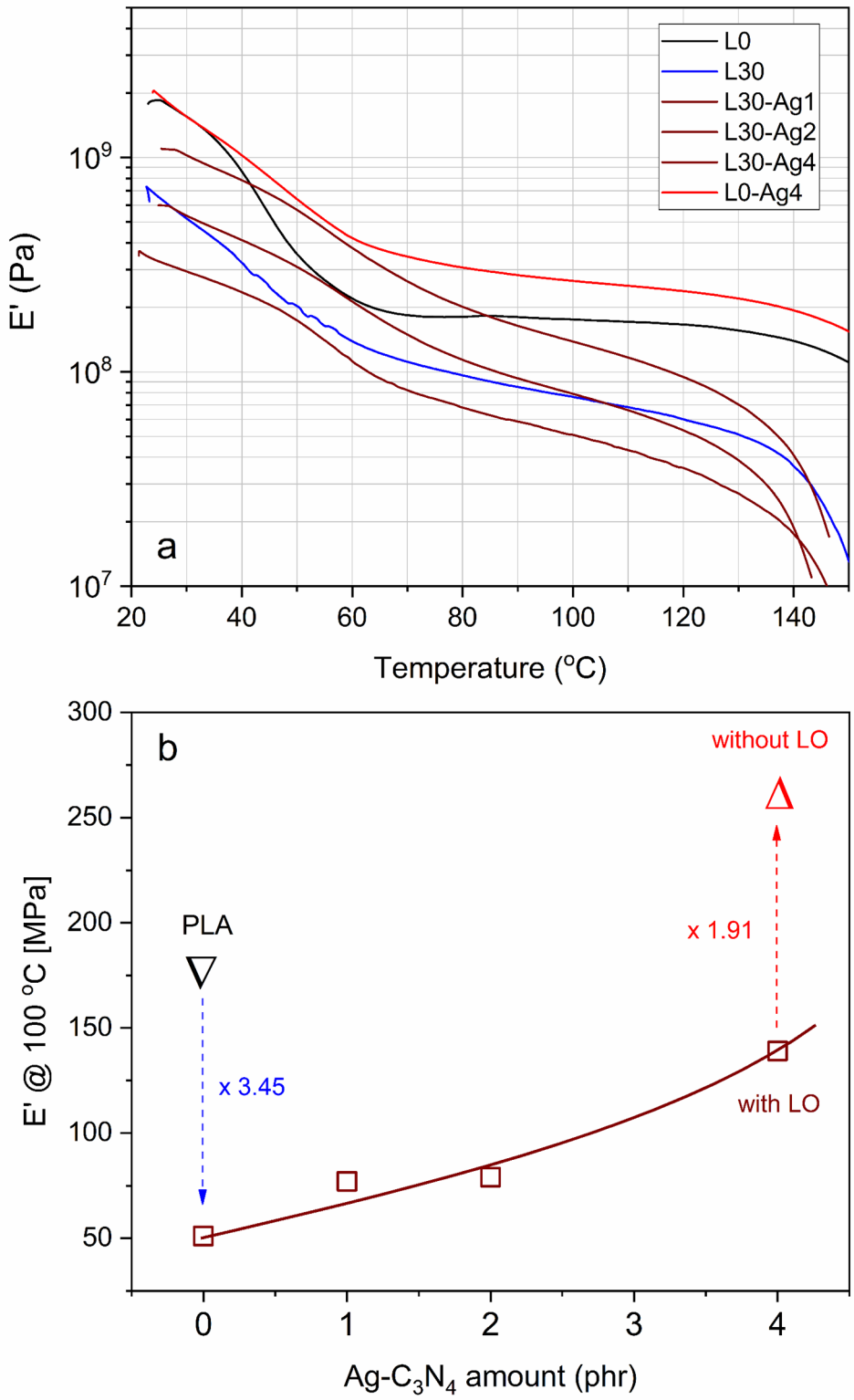

Fig. 10 (a) Storage modulus (E') curves of samples as a function of temperature and (b) E' values of samples at a particular temperature in rubbery region

Table 4 Antibacterial activity of samples against pathogenic microorganisms

Samples	Inhibition Zone (mm)		
	A. baumannii	*E. coli*	*S. aureus*
L0 (PLA)	0	0	0
L30	0	0	0
L30-Ag1	12	12	14
L30-Ag2	11	7	13
L30-Ag4	11	13	14
L0-Ag4	11	11	13
AMC[a]	19	-	-
AMC[a]	-	35	-
VA[b]	-	-	17

[a] AMC: amoxicillin-clavulanate (20/10 µg/ml)

[b] VA: vancomycin (30 µg/ml)

This lipopolysaccharide and protein part are more resistant to EOs [46].

Nowadays, a significant increase has been observed in foodborne diseases. This condition is often associated with raw food consumption. It is known that the bacteria used in this study cause foodborne infections. A. baumannii is associated with multidrug resistance (MDR) and has been reported to be detected in animal foods and vegetables [47, 48]. It has been concluded that our findings on the antibacterial activity against A. baumannii make a significant contribution to the existing literature. It was also observed that the L0 (PLA) and L30 films did not exhibit any antibacterial activity on S. aureus, A. baumannii, and E. coli bacteria. However, the literature suggests that L. orientalis extracts have antibacterial activity [49–53]. Another crucial point of the current study is the fact that the introducing the combinations of L. orientalis oil and 2D designed antibacterial agent (Ag@g-C3N4) into PLA showed better antibacterial activity than the only antibacterial agent loaded film (L0-Ag4). This indicates that the synergy between silver and L. orientalis extract enhances the antibacterial activity.

Conclusions

This study reports the structure-property relationships of flexible antibacterial PLA-based films formulated by using *L. orientalis* oil as a bio-based and sustainable plasticizer harvested from an endemic Anatolian sweetgum tree. Additionally, composite films containing PLA and 2D g-C_3N_4 sheets decorated with Ag nanoparticles were prepared. It has been shown that Ag nanoparticles with an average diameter of 10–30 nm were synthesized by in-situ chemical reduction onto the 2D nano sheets. Then a functional additive, Ag@g-C_3N_4 nanocomposite, was successfully obtained and used as antibacterial agent into a thermoplastic matrix. Furthermore, it has been shown that *L. orientalis* oil plasticized the PLA and significantly reduced its glass transition temperature. *L. orientalis* oil also acted as an agent to improve the dispersion of nanocomposite particles into the PLA matrix and enhanced the antibacterial activity of the Ag@g-C_3N_4 nanocomposite. It can be concluded that a PLA-based nanocomposite, possessing a composition of PLA/*L. orientalis* oil/Ag@g-C_3N_4 (100/30/2), could be successfully used in various engineering applications that requires antibacterial and biodegradable plastic parts such as food packaging films, medical materials like tissue scaffolds, textile and automotive plastics etc.

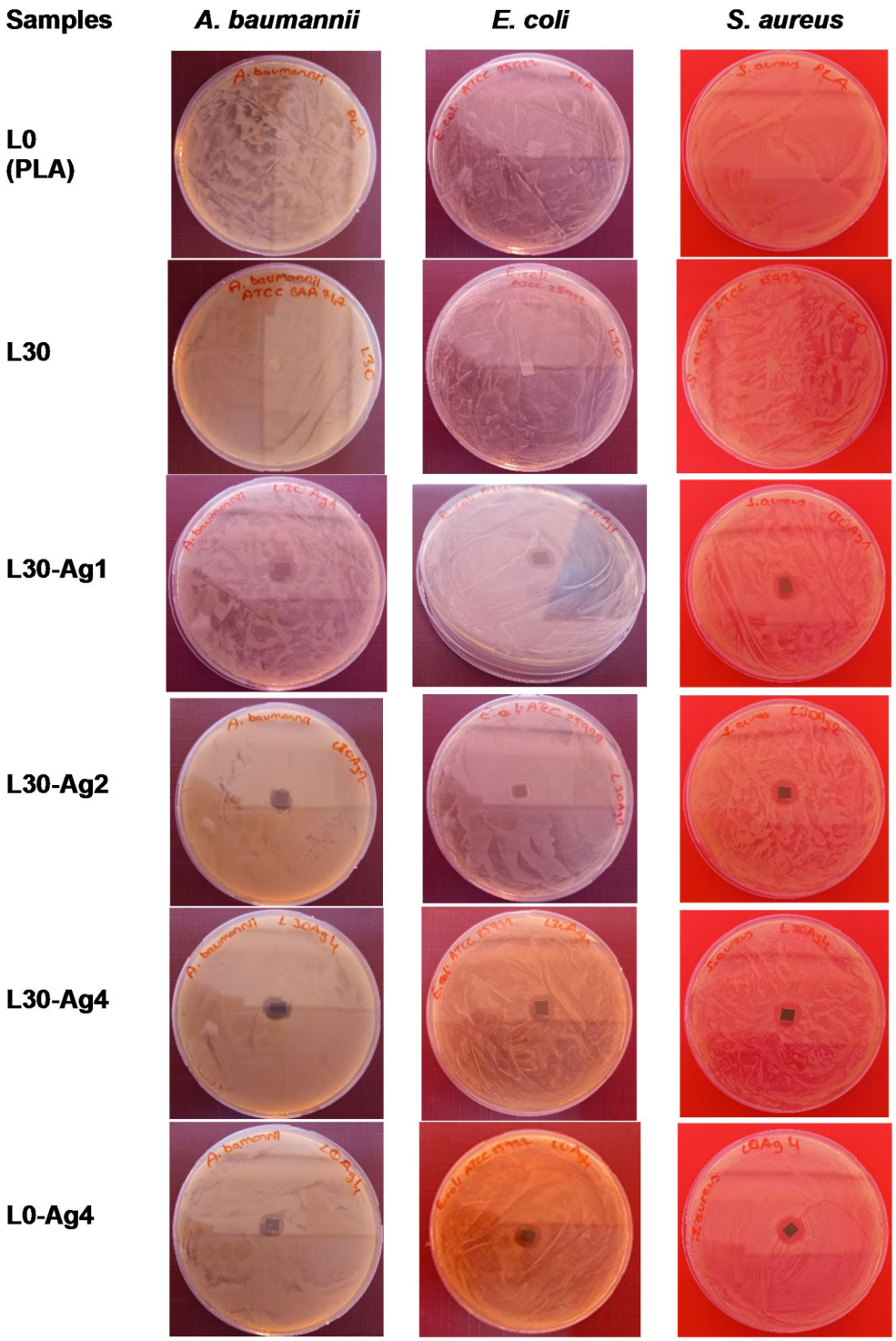

Fig. 11 Photographs of inhibition zones of samples and antibiotics as the control samples against three different pathogenic microorganisms

Acknowledgements Financial supports received from the MLU Halle-Wittenberg and from the BMBF (Grant number FKZ:03Z22HN11) are greatly acknowledged.

Author Contributions Author 1 tooks part in "Conceptualization", "Data Curation", "Investigation", "Methodology in material synthesis work" and "Writing – original draft" Authors 2, 3, and 4 made "Investigation in characterization/analysis studies", "Formal analysis", and "Writing – original draft" Author 5 was responsible for "Funding acquisition", "Project administration" and "Writing – review & editingAuthor 6 (corresponding author) made "reviewing and editing original draft", "Supervision", and "Conceptualization".

Funding Open access funding provided by the Scientific and Technological Research Council of Türkiye (TÜBİTAK).

Data Availability No datasets were generated or analysed during the current study.

Declarations

Conflict of interest There are no conflicts to declare.

References

1. Awal A, Rana M, Sain M (2015) Thermorheological and mechanical properties of cellulose reinforced PLA bio-composites. Mech Mater 80(Part A):87–95
2. Enumo A, Gross IP, Saatkamp RH, Pires AT, Parize AL (2020) Evaluation of mechanical, thermal and morphological properties of PLA films plasticized with maleic acid and its propyl ester derivatives. Polym Test 88:106552
3. Gao C, Chen P, Ma Y, Sun L, Yan Y, Ding Y, Sun L (2023) Multifunctional polylactic acid biocomposite film for active food packaging with UV resistance, antioxidant and antibacterial properties. Int J Biol Macromol 253(1):126494
4. Ren JZ, Li YA, Lin QB, Li ZH, Zhang GQ (2022) Development of biomaterials based on plasticized polylactic acid and tea polyphenols for active-packaging application. Int J Biol Macromol 217:814–823
5. Ljungberg N, Wesslen B (2003) Tributyl citrate oligomers as plasticizers for poly (lactic acid): thermo-mechanical film properties and aging. Polymer 44(25):7679–7688
6. Maiza M, Benaniba MT, Quintard G, Massardier-Nageotte V (2015) Biobased additive plasticizing polylactic acid (PLA). Polimeros 25:581–590
7. Maiza M, Benaniba MT, Massardier-Nageotte V (2016) Plasticizing effects of citrate esters on properties of poly (lactic acid). J Polym Eng 36(4):371–380
8. Gzyra-Jagieła K, Sulak K, Draczyński Z, Kiełbik LM, Jagodzińska S, Borkowski D (2022) Influence of the structure of low molecular weight esters on poly (lactic acid) in the plasticization process-part 1. Fibres Text East Eur 30(3):93–101
9. Martino VP, Jiménez A, Ruseckaite RA (2009) Processing and characterization of poly (lactic acid) films plasticized with commercial adipates. J Appl Polym Sci 112(4):2010–2018
10. Al-Mulla EAJ, Yunus WMZW, Ibrahim NAB, Rahman MZA (2010) Properties of epoxidized palm oil plasticized polytlactic acid. J Mater Sci 45:1942–1946
11. Tee YB, Talib RA, Abdan K, Chin NL, Basha RK, Yunos KFM (2016) Comparative study of chemical, mechanical, thermal, and barrier properties of poly (lactic acid) plasticized with epoxidized soybean oil and epoxidized palm oil. BioResources 11(1):1518–1540
12. Hassouna F, Raquez JM, Addiego F, Dubois P, Toniazzo V, Ruch D (2011) New approach on the development of plasticized polylactide (PLA): grafting of poly (ethylene glycol) (PEG) via reactive extrusion. Eur Polymer J 47(11):2134–2144
13. Mele G, Bloise E, Cosentino F, Lomonaco D, Avelino F, Marcianò T, Massaro C, Mzetto SE, Tammaro L, Scalone AG, Schioppa M, Terzi R (2019) Influence of cardanol oil on the properties of poly (lactic acid) films produced by melt extrusion. ACS Omega 4:718–726
14. Carpintero M, Marcet I, Rendueles M, Díaz M (2021) Egg yolk oil as a plasticizer for polylactic acid films. Membranes 12(1):46
15. Hasanoglu Z, Sivri N, Alanalp MB, Durmus A (2024) Preparation of polylactic acid (PLA) films plasticized with a renewable and natural *Liquidambar orientalis* oil. Int J Biol Macromol 257:128631
16. Gao F, Mi Y, Wu X, Yao J, Qi Q, Chen W, Cao Z (2022) Preparation of quaternized chitosan/Ag composite nanogels in inverse miniemulsions for durable and antimicrobial cotton fabrics. Carbohydr Polym 278:118935
17. Martorana A, Pitarresi G, Palumbo FS, Catania V, Schillaci D, Mauro N, Fiorica C, Giammona G (2022) Fabrication of silver nanoparticles by a diethylene triamine-hyaluronic acid derivative and use as antibacterial coating. Carbohydr Polym 295:119861
18. Liu C, Ling J, Yang L-Y, Ouyang X-k, Wang N (2023) Chitosan-based carbon nitride-polydopamine–silver composite dressing with antibacterial properties for wound healing. Carbohydr Polym 303:120436
19. Fortunati E, Peltzer M, Armentano I, Jiménez A, Kenny JM (2013) Combined effects of cellulose nanocrystals and silver nanoparticles on the barrier and migration properties of PLA nano-biocomposites. Carbohydr Polym 118(1):117–124
20. Fortunati E, Armentano I, Zhou Q, Iannoni A, Saino E, Visai L, Berglund LA, Kenny JM (2012) Multifunctional bionanocomposite films of poly(lactic acid), cellulose nanocrystals and silver nanoparticles. Carbohydr Polym 87:1596–1605
21. Yalcinkaya EE, Puglia D, Fortunati E, Bertoglio F, Bruni G, Visai L, Kenny JM (2017) Cellulose nanocrystals as templates for cetyltrimethylammoniumbromide mediated synthesis of Ag nanoparticles and their novel use in PLA films. Carbohydr Polym 157:1557–1567
22. Velásquez E, Patiño Vidal C, Rojas A, Guarda A, Galotto MJ, de López C (2021) Natural antimicrobials and antioxidants added to polylactic acid packaging films. Part I: polymer processing techniques. Compr Rev Food Sci Food Saf 20(4):3388–3403
23. Durmus Z, Köferstein R, Lindenberg T, Lehmann F, Hinderberger D, Maijenburg AW (2023) Preparation and characterization of Ce-MOF/g-C_3N_4 composites and evaluation of their photocatalytic performance. Ceram Int 49:24428–24441
24. Sarangapany S, Mohanty K (2021) Facile green synthesis of Ag@g-C_3N_4 for enhanced photocatalytic and catalytic degradation of organic pollutant. J Cluster Sci 32:585–592
25. Zhu H, Wu K-J, He C-H (2022) Ultrasound-assisted synthesis of visible-light-driven Ag/g-C_3N_4 catalysts in a continuous flow reactor. Chem Eng J 429:132412
26. Fischer EW, Sterzel HJ, Wegner G (1973) Investigation of the structure of solution grown crystals of lactide copolymers by means of chemical reactions. Kolloid-Z u Z Polymere 251:980–990
27. Wen P, Zhu DH, Wu H, Zong MH, Jing YR, Han SY (2016) Encapsulation of cinnamon essential oil in electrospun nanofibrous film for active food packaging. Food Control 59:366–376
28. Shahid MA, Ali A, Uddin MN, Miah S, Islam SM, Mohebbullah M, Jamal MSI (2021) Antibacterial wound dressing electrospun nanofibrous material from polyvinyl alcohol, honey and *curcumin longa* extract. J Ind Text 51(3):455–469
29. Zhang JS, Chen XF, Takanabe K, Maeda K, Domen K, Epping JD, Fu XZ, Antonietti M, Wang XC (2010) Synthesis of a carbon nitride structure for visible-light catalysis by copolymerization. Angew Chem Int Ed 49(2):441–444

30. Yan SC, Li ZS, Zou ZG (2009) Photodegradation performance of g-C_3N_4 fabricated by directly heating melamine. Langmuir 25(17):10397–10401
31. Yue B, Li QY, Iwai H, Kako T, Ye JH (2011) Hydrogen production using zinc-doped carbon nitride catalyst irradiated with visible light. Sci Technol Adv Mater 12(3):034401
32. Chang F, Xie Y-C, Li C, Chen J, Luo J, Hu X-F, Shen J-W (2013) A facile modification of g-C_3N_4 with enhanced photocatalytic activity for degradation of methylene blue. Appl Surf Sci 280:967–974
33. Durmus A, Koc SN, Pozan GS, Kasgoz A (2005) Thermal-catalytic degradation kinetics of polypropylene over BEA, ZSM-5 and MOR zeolites. Appl Catal B 61:316–322
34. Gauri B, Vidya K, Sharada D, Shobha W (2016) Synthesis and characterization of Ag/AgO nanoparticles as alcohol sensor. Res J Chem Environ 20(10):1–5
35. Hovaneissian M, Archier P, Mathe C, Vieillescazes C (2006) Contribution De La Chimie Analytique à l'étude Des Exsudats végétaux styrax, Storax et benjoin. C R Chim 9(9):1192–1202
36. Demir D, Özdemir S, Ceylan S, Yalcin MS, Sakım B, Bölgen N (2022) Electrospun composite nanofibers based on poly (ε-caprolactone) and styrax liquidus (Liquidambar orientalis Miller) as a wound dressing: preparation, characterization, biological and cytocompatibility results. J Polym Environ 30(6):2462–2473
37. Arslan MB, Şahin HT (2016) A forgotten forest product source: Anatolian sweetgum tree (Liquidambar Orientalis Miller). J Bartın Fac Forestry 18(1):103–117
38. Bitinis N, Verdejo R, Maya EM, Espuche E, Cassagnau P, Lopez-Manchado MA (2012) Physicochemical properties of organoclay filled polylactic acid/natural rubber blend bionanocomposites. Compos Sci Technol 72:305–313
39. Laput O, Vasenina I, Salvadori MC, Savkin K, Zuza D, Kurzina I (2019) Low-temperature plasma treatment of polylactic acid and PLA/HA composite material. J Mater Sci 54:11726–11738
40. McShan D, Ray PC, Yu H (2014) Molecular toxicity mechanism of nanosilver. J Food Drug Anal 22(1):116–127
41. Luther EM, Schmidt MM, Diendorf J, Epple M, Dringen R (2012) Upregulation of metallothioneins after exposure of cultured primary astrocytes to silver nanoparticles. Neurochem Res 37(8):1639–1648
42. Burt S (2004) Essential oils: their antibacterial properties and potential applications in foods-a review. Int J Food Microbiol 94(3):223–253
43. da Silva Dannenberg G, Funck GD, dos Santos Cruxen CE, de Lima Marques J, da Silva WP, Fiorentini ÂM (2017) Essential oil from pink pepper as an antimicrobial component in cellulose acetate film: potential for application as active packaging for sliced cheese. LWT-Food Sci Technol 81:314–318
44. da Silva FT, da Cunha KF, Fonseca LM, Antunes MD, Halal E, Fiorentini SLM, Â. M., Dias ARG (2018) Action of ginger essential oil (Zingiber officinale) encapsulated in proteins ultrafine fibers on the antimicrobial control in situ. Int J Biol Macromol 118:107–115
45. do Evangelho JA, da Silva Dannenberg G, Biduski B, Halal E, Kringel SLM, Gularte DH, M. A., da Zavareze R, E (2019) Antibacterial activity, optical, mechanical, and barrier properties of corn starch films containing orange essential oil. Carbohydr Polym 222:114981
46. Yang T, Qin W, Zhang Q, Luo J, Lin D, Chen H (2023) Essential-oil capsule preparation and its application in food preservation: a review. Food Reviews Int 39(7):4124–4158
47. Marí-Almirall M, Cosgaya C, Pons MJ, Nemec A, Ochoa TJ, Ruiz J, Vila J (2019) Pathogenic Acinetobacter species including the novel Acinetobacter dijkshoorniae recovered from market meat in Peru. Int J Food Microbiol 305:108248
48. Almasaudi SB (2018) Acinetobacter spp. as nosocomial pathogens: epidemiology and resistance features. Saudi J Biol Sci 25(3):586–596
49. Sagdic O, Ozkan G, Ozcan M, Ozcelik S (2005) A study on inhibitory effects of Sweet gum Tree (Liquidambar orientalis Mill. Var. Orientalis) storax against several bacteria. Phytotheraphy Res 19(6):549–551
50. Kim J, Seo SM (2008) Nematicidal activity of plant essential oils and components from coriander (Coriandrum sativum), oriental sweetgum (Liquidambar orientalis), and valerian (Valeriana Wallichii) essential oils against pine wood nematode (Bursaphelenchus Xylophilus). J Agric Food Chem 56:7316–7320
51. Oskay M, Oskay D, Kalyoncu F (2009) Activity of some plant extracts against multi-drug resistant human pathogens. Iran J Pharm Res 8:293–300
52. Okmen G, Turkcan O, Gork G (2014) The antimicrobial activity of Liquidambar orientalis Mill against food pathogens and antioxidant capacity of leaf extracts. Afr J Tradit Complement Altern Med 11:28−32
53. Yasmin H, Kaiser MA, Sarker MMR, Rahman MS, Rashid MA (2010) Preliminary anti-bacterial activity of some indigenous plants of Bangladesh. Dhaka Univ J Pharm Sci 8:61−65